The role of riverine bed roughness, egg pocket location, and egg pocket permeability on salmonid redd-induced hyporheic flows

Bishal Bhattarai[1]*, Brandon Hilliard[2], William J. Reeder[2], Ralph Budwig[2], Benjamin T. Martin[3], Tao Xing[1] and Daniele Tonina[2]*

1. Department of Mechanical Engineering, University of Idaho, Idaho, USA
2. Center for Ecohydraulics Research, University of Idaho, Idaho, USA
3. Institute for Biodiversity and Ecosystem Dynamics, University of Amsterdam, Amsterdam, the Netherlands

*Corresponding Authors

ABSTRACT

Salmon spawning activities alter streambed morphology, forming a dune-shaped egg nest called a redd. The spawning process increases redd sediment hydraulic conductivity, K_D, and congregates large sediment grains to form an egg pocket, such that egg pocket hydraulic conductivity, K_{EP}, may be higher than K_D. Salmon females may create one or more egg pockets within a single redd. Although the impact of redd shape and K_D on redd-induced hyporheic fluxes has been studied, the effects of streambed roughness, R, egg pocket permeability, and egg pocket location on egg pocket hyporheic fluxes, $\bar{q}_{ep}$, (downwelling flows from the stoss side of the redd which may enter egg pockets) have not yet been quantified. This study investigates this knowledge gap with a set of numerical simulations supported by flume experiments. We simulated hyporheic flows for five egg pocket locations, five K_{EP} values from 0.0025 to 0.02 m/s, and 12 rough streambed surfaces. Surface roughness was scaled from a measured streambed surface in two ways - only vertically (R_1) and both vertically and horizontally (R_2) - with scaling coefficients ranging from 0.5 to 3. The measured streambed surface had a median diameter, D_{50}, of 1 cm and a standard deviation (σ_D) of 0.77 cm. The results indicated that the dimensionless flux into the egg pocket, $\bar{q}_{ep}^{*} = \frac{\bar{q}_{ep}}{K_D}$ increases noticeably with the downstream distance of egg pockets from the redd pit, and less strongly with ${K_{EP}}^{*} = \frac{K_{EP}}{K_D}$. The near-surface downwelling fluxes significantly increase with R_1, but only negligibly with R_2, and for deeper egg pockets, $\bar{q}_{ep}^{*}$ is minimally impacted by surface roughness. Our results suggest that the typical simplification of a smooth redd surface with a single redd hydraulic conductivity accurately represents the interstitial flow within the redd, and the effects of surface roughness and egg pocket hydraulic conductivity on $\bar{q}_{ep}^{*}$ fall within the uncertainty of the egg pocket location.

Keywords:

hydraulic conductivity, hyporheic zone, salmon redd, egg pockets, waterbed roughness

1. INTRODUCTION

Female salmonids bury their eggs within the hyporheic zone of gravel-bed rivers (Baxter & Hauer, 2000). They create egg nests, called redds, by excavating a pit in the streambed gravel and then covering the fertilized eggs with sediment from a second pit (Burner, 1951; Chapman, 1988; Crisp & Carling, 1989; Deverall et al., 1993; Groot & Margolis, 1991). This process results in a topographical feature similar to a dune, with a pit and hump called a tailspill (Bjornn & Reiser, 1991) (Figure 1). The spawning-related activity leads to the redd having a higher hydraulic conductivity, K_D, than the undisturbed streambed sediments, K_{UD}, due to the removal of fine grains and loosening of the sediment matrix (Coble, 1961; Merz et al., 2004; Tappel & Bjornn, 1983; Zimmermann & Lapointe, 2005b). Salmonids form the egg pocket by clustering the larger sediment where they lay their eggs (Peterson & Quinn, 1996). This egg pocket has an average size of 7 to 10 cm and may exhibit higher hydraulic conductivity, K_{EP}, than that of the redd (Kondolf, 2000; McNeil & Ahnell, 1964). This higher permeability can benefit embryos because it increases hyporheic flows, bringing oxygen-rich surface water to the egg pocket (Tonina & Buffington, 2009). These hyporheic fluxes are assumed to be chiefly induced by the dune-like shape of the redd, which causes downwelling fluxes in the pit and upwelling fluxes downstream of the tailspill crest (Cardenas et al., 2016; Tonina & Buffington, 2009).

Female salmonids can form multiple egg pockets within a single redd (Van Den Berghe & Gross, 1984; Crisp & Carling, 1989; Elliott, 1984; Hawke, 1978; Maekawa & Hino, 1990). Therefore, the location of egg deposition may vary within the redd, mainly between the pit and the tailspill crest (Crisp & Carling, 1989) (Figure 1). Despite these observations, research has treated redds as a homogenous feature without investigating the effects of egg pocket permeability and location on hyporheic fluxes to the incubating embryos.

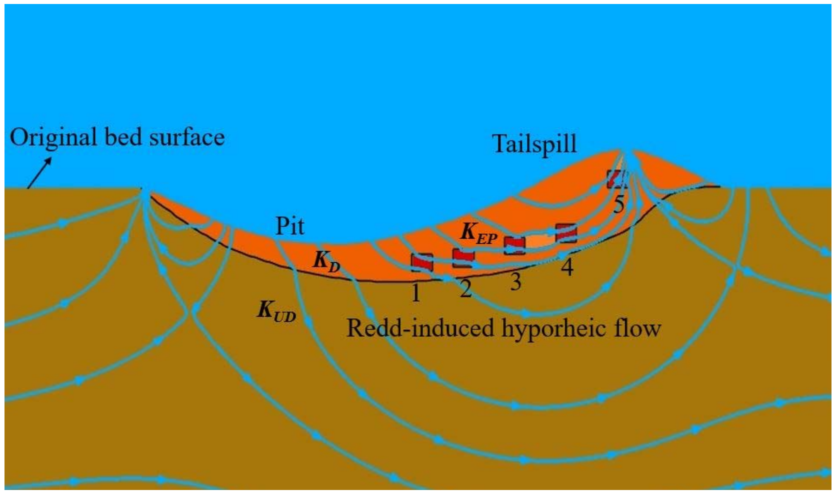

Figure 1: Schematic of the longitudinal profile of a redd with the five egg pockets (labeled 1 to 5- highlighted in red) of hydraulic conductivity (K_{EP}), located in the disturbed sediment (orange) of hydraulic conductivity (K_D). The brown color indicates the undisturbed streambed material of hydraulic conductivity (K_{UD}). Streamlines show the flow paths.

Similarly, previous research (Cardenas et al., 2016; Tonina & Buffington, 2009) considered the redd shape as a smooth surface without taking into account the surface roughness (Evenson, 2001). Gravel-bed streams have broad grain size distributions, which create uneven surfaces characterized by grain-scale roughness (Heritage & Milan, 2009; Keulegan, 1938; Whiting & Dietrich, 1991; Wiberg & Smith, 1991). This roughness can be quantified with the standard deviation of the bed elevation, detrended from the large-scale variability caused by various bedforms (Aberle & Nikora, 2006; Cooper & Tait, 2009; Nikora et al., 1998; Smart et al., 2004).

Early studies investigated how granular porous beds affect underground water flow, causing water to move slower within the gravel from the surface due to head variations generated by grain-scale roughness, which in turn promotes the momentum exchange between the surface and subsurface waters (Greig S. M. et al., 2006; Mendoza & Zhou, 1992; Zhou & Mendoza, 1993). This roughness drives microhabitat-scale exchange, resulting in surface water penetrating shallower depths and flow paths being shorter compared to bedform-driven hyporheic exchange (Hervant & Malard, 1999).

However, limited information is available regarding the impact of surface roughness on hyporheic fluxes induced by redds and how they may impact hyporheic fluxes deeper in the redd, near the potential locations of egg pockets. Surface roughness may affect the downwelling flux entering the redd but may not impact the flow reaching the egg pockets, as they may be located at depths greater than the hyporheic flow cells induced by grain-scale roughness. Consequently, we hypothesize that, even in the presence of grain-induced hyporheic flows, the flow to the egg pocket is primarily influenced by the redd-scale hyporheic flow.

The present study aims to address this hypothesis by investigating the impact of egg pocket hydraulic conductivity, their locations, the effect of multiple egg pockets within a redd, and surface roughness on redd-induced hyporheic fluxes. We used a set of numerical modeling techniques, constrained by field information, to simulate and analyze surface and subsurface flows in a two-dimensional (2D) numerical hydraulic model. The models are linked through the near-bed pressure distribution, which is quantified using a two-phase (air-water) computational fluid dynamics model for surface water. We applied this modeling approach to a typical Chinook salmon (*Oncorhynchus tshawytscha*) redd under surface flow conditions observed in the Sacramento River.

2. METHODS

2.1 Surface flow hydraulics

We used the two-dimensional (2D) surface model developed by Bhattarai et al. (2023) (In Press) to simulate open channel flow surface hydraulics over a salmon redd. The model employed a two-phase (air-water) solver for the Reynolds-Averaged Navier-Stokes (RANS) equations with a κ-ε realizable turbulence closure scheme in ANSYS. The volume of fluid (VOF) approach was applied to extract the water surface profile where the volume fraction is 0.5, with the values of 1 or 0 indicating only water or air, respectively. A long flow domain was utilized to develop and train the flow, which included two fixed-lid sections upstream and downstream of a 45 m long two-phase domain. The water-sediment interface was specified as a no-slip impermeable boundary (Cardenas & Wilson, 2007b, 2007a; Chen et al., 2015) since momentum and mass exchanges with porous sediment are considered negligible (Janssen et al., 2012). Water boundaries were defined as velocity inlet and velocity outlet conditions for the upstream and downstream locations, respectively, while air boundaries were specified as pressure outlets (Figure S1). The model domain consisted of approximately two million quadrilateral cells, with a mean cell size of about 2.4 cm in the horizontal direction. To accurately track the water surface elevation, a highly refined vertical cell size of 1.6 mm was employed at the air-water interface. Additionally, a very small vertical cell size of approximately 0.06 mm was used near the bottom boundary. The flow was characterized by a mean slope of 0.007%, an average velocity of 1.49 m/s, and a mean depth of 3.92 m. These values were measured at a location with redds along the Sacramento River and correspond to run number 14 in Table 4 of Bhattarai et at., (2023) (In

Press). The water-sediment surface was characterized by 12 rough cases and a smooth case, which was used as a reference condition (see Section Streambed roughness).

2.2 Groundwater flow hydraulics

The hyporheic flow was simulated with the steady-state Darcian solver in ANSYS within a 2D domain, similar to the method employed by Bhattarai et al. (2023) (In Press). The upper boundary of the domain was defined as the pressure inlet boundary, with the pressure distribution at the water-sediment interface predicted by the RANS surface model. The bottom boundary was treated as an impermeable slip wall boundary located 5 m below the water-sediment interface to avoid affecting the hyporheic flow cell induced by the redd. A periodic boundary condition was applied at the upstream and downstream locations of the subsurface domain boundaries. This boundary condition imposed an ambient groundwater flow of approximately 0.001 mm/s, mimicking a large-scale longitudinal groundwater flow from a valley slope. The computational mesh used has an average grid cell size of 2.5 cm horizontally and 3 cm vertically, resulting in approximately 500,000 quadrilateral cells. The hydraulic conductivity for the undisturbed bed, K_{UD}, was set to 0.0005 m/s, representing the surrounding streambed material, while the hydraulic conductivity for the disturbed bed, K_D, was set to 0.0025 m/s, representing the permeability of the redd bedform.

2.3 Egg pocket characteristics

We simplified the chinook salmon egg pocket by using a rectangular shape measuring 10 cm in length and 7 cm in height, corresponding to the average dimensions observed by Evenson (2001). The hydraulic conductivity of the egg pocket, K_{EP}, is higher than that of K_D (Chapman, 1988). The mean hydraulic conductivity for fall Chinook salmon spawning areas ranged from 0.009 to 0.21 cm/s in the Hells Canyon Reach of the Snake River and 0.005 cm/s, with a maximum value of 0.043 cm/s, in the Hanford Reach of the Columbia River (Hanrahan et al., 2005). Geist (2000) estimated hydraulic conductivity values ranging from 0.02 – 0.03 cm/s near fall Chinook salmon spawning areas in the Hanford Reach. In the Columbia River, Chapman (1988) and Zimmermann and Lapointe (2005a) observed a hydraulic conductivity value of 2.9 cm/s in the chinook salmon redds. Based on this information, we analyzed the effect of varying K_{EP} from 0.0025 m/s to 0.02 m/s. We defined the index ${K_{EP}}^* = \frac{K_{EP}}{K_D}$, which varied between 1 and 8, to study the effect of different hydraulic conductivities between the egg pocket and redd.

The impact of egg pocket location on the spatial average interstitial fluxes entering the egg pocket, $\bar{q}_{ep}$, was investigated by analyzing five egg pockets located both independently and collectively within a single redd (Crisp & Carling, 1989) (Figure 2). The horizontal distances of the upstream ends of the five egg pockets from the upstream end of the redd are 1.3 m, 1.5 m, 1.75 m, 2 m, and 2.25 m, respectively. The top of egg pockets EP_1, EP_2, EP_3, and EP_4 are situated 27 cm, 25 cm, 20 cm, and 15 cm, respectively, below the original bed surface, while the top of EP_5 is situated 7 cm above the original bed surface near the tailspill of the redd.

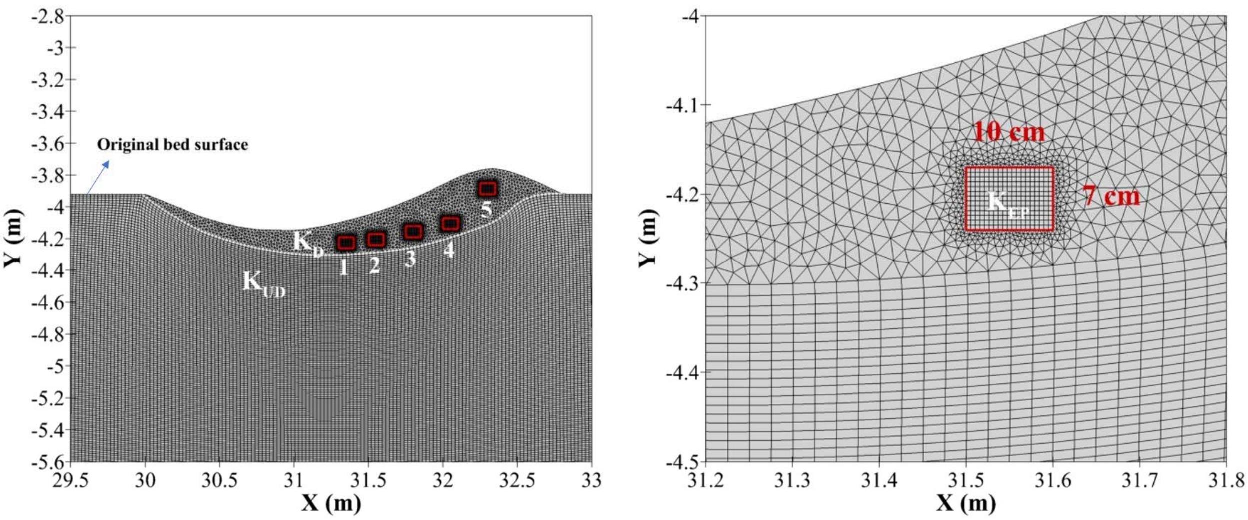

(a) (b)

Figure 2: Redd disturbed (K_D) and undisturbed (K_{UD}) sediment along with the (a) five egg pockets positioned left to right, EP_1 to EP_5, and (b) EP_2, showing the dimensions of the egg pocket.

2.4 Streambed roughness

Natural streambed roughness varies across sites and flows due to its dependence on multiple factors, including grain shape, orientation, packing, spacing, and vertical and structural arrangements (Nikora et al., 1998). In this study, we used a 5 mm survey of a plane gravel bed surface that was water-worked in a flume. The grain size distribution of the bed had a median grain size of 10 mm and a standard deviation of 7.7 mm (Dudunake et al., 2020). This original rough surface served as the baseline from which we created two types of roughness by scaling the vertical and horizontal distances using six constant multipliers: 0.5, 1, 1.5, 2, 2.5, and 3.

To generate a highly rough surface, referred to as the R_1 roughness type (Figure 3a), we scaled the surface only vertically, which exaggerates the vertical protrusion of the grains. This may represent an extreme case where the grains have their b axes vertically aligned, as observed in the analysis conducted by Lee et al. (2020). In contrast, the R_2 roughness represents a more natural roughness, achieved by scaling both vertically and horizontally with the same scaling factor (Figure 3b). Since we geometrically scaled the surface for the R_2 type, it is equivalent to increasing the grain size distribution such that the median grain size corresponds to 0.5, 1, 1.5, 2, 2.5, and 3 cm. We analyzed a total of six different rough beds, in addition to a smooth bed, for both R_1 and R_2, with streambed elevation standard deviations, σ_E, of 2, 4.4, 6.7, 8.9, 11, and 13.3 mm (Figure 3).

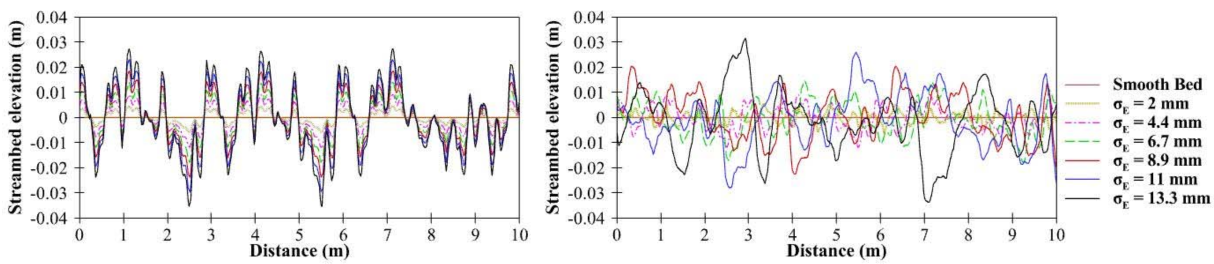

(a) (b)

Figure 3: Zoom-in section of the streambed profiles (a) R_1 and (b) R_2.

3. DATA ANALYSIS

To quantify the impact of the selected three treatments - surface roughness, egg pocket location, and egg pocket hydraulic conductivity - on the hyporheic fluxes, we analyzed the downwelling fluxes at various locations. We defined the mean spatial downwelling fluxes at the water-sediment interface as $\bar{q}_d$, representing the overall water exchange induced by the redd, and as $\bar{q}_{d,ep}$, representing the downwelling fluxes through the stoss side of the redd flowing toward the area where egg pockets are most likely located. These fluxes were obtained by averaging the fluxes over the downwelling area. Similarly, we defined $\bar{q}_{ep}$ as the mean spatial flux entering the egg pocket, which represents the embryos habitat. We also defined the mean spatial downwelling fluxes over the surfaces located at a depth two times ($\bar{q}_{d,2d,ep}$) and three times ($\bar{q}_{d,3d,ep}$) the D_{50} of roughness ($\sigma_E = 13.3\ mm$) value below the redd surface. These two fluxes represent the overall hyporheic flow that affects the area within the redd where egg pockets are primarily located. To eliminate the influence of hydraulic conductivity on the fluxes, we normalized them by the redd hydraulic conductivity (K_D): $\bar{q}_d^* = \frac{\bar{q}_d}{K_D}$ (dimensionless downwelling mean flux over the entire redd), $\bar{q}_{ep}^* = \frac{\bar{q}_{ep}}{K_D}$ (dimensionless mean flux entering an egg pocket), $\bar{q}_{d,ep}^* = \frac{\bar{q}_{d,ep}}{K_D}$ (dimensionless downwelling mean flux toward the egg pockets at the water-sediment interface), $\bar{q}_{d,2d,ep}^* = \frac{\bar{q}_{d,2d,ep}}{K_D}$ (dimensionless downwelling mean flux toward the egg pockets at a surface located 2 times the median grain size below the streambed location), $\bar{q}_{d,3d,ep}^* = \frac{\bar{q}_{d,3d,ep}}{K_D}$ (dimensionless downwelling mean flux toward the egg pockets at a surface located 3 times the median grain size below the streambed location).

4. MODEL PERFORMANCE

Bhattarai et al. (2023) (In Press) quantified the model's performance against flume experiments conducted on a redd with a smooth surface. They evaluated the agreement using the Nash-Sutcliffe coefficient (NSC), which quantifies the performance of a CFD model. The NSC values indicate the degree of agreement and are classified as follows: very good (NSC > 0.75), good (0.65 < NSC ≤ 0.75), satisfactory (0.5 < NSC ≤ 0.65), or unsatisfactory (NSC ≤ 0.5) (Moriasi et al., 2007). For the smooth bed, the model performance was very good for a set of two mean flow depths (0.1 and 0.2 m) and velocities (0.1 and 0.2 m/s) (Figure 4 of Bhattarai et al. (2023) (In Press)).

To evaluate the model's performance under rough bed conditions, we conducted two flume experiments using a streambed surface rougher than those in Bhattarai et al. (2022) (In Press), while maintaining a similar redd size and shape (a 1/3 scaled version of an average Chinook salmon redd) in a 7 m long, 0.5 m wide, and 0.7 m deep recirculating flume. Experiments had slow (0.1 m/s) and fast (0.2 m/s) flow velocities and one mean flow depth of 0.1 m. The two velocities were near those observed at redd locations (Deverall et al., 1993). The model redd was constructed with non-spherical tetrafluoroethylene hexafluoropropylene vinylidene fluoride (THV) grains, produced by 3M, with an average diameter of 3 mm. The surface roughness of the model redd was achieved by placing a mixture of molded THV grains with different nominal diameters (7, 14, and 17 mm) on the bed. The specific gravity of the THV grains was approximately 2 with a refractive index (RI) of around 1.365. Matching the refractive index of the THV grains and the fluid allowed us to employ the non-intrusive imaging technique of stereo particle image velocimetry (SPIV). To achieve the RI match, we mixed fresh water with magnesium sulfate at a proportion of 15% by weight, causing the model salmon redd to be transparent once saturated. To minimize potential boundary effects, the redd was positioned in the middle of the flume. The inflowing water was directed through a flow straightener before entering the flume, and a weir gate was used to regulate the downstream boundary.

We utilized SPIV to map the flow field downstream of the redd crest, where complex hydraulics occur, to validate our CFD model. The starting of the redd is at $X = 0$. Upstream flow field measurements ($X = -2.04$ m) were taken to establish boundary conditions for streamwise (V_x) and vertical (V_y) velocities (V_y constituted less than 2% of V_x), as well as turbulence kinetic energy (*TKE*) profiles for the CFD models. At the downstream boundary ($X = 2$ m), a pressure outlet was applied with a hydrostatic pressure profile (Figure S2).

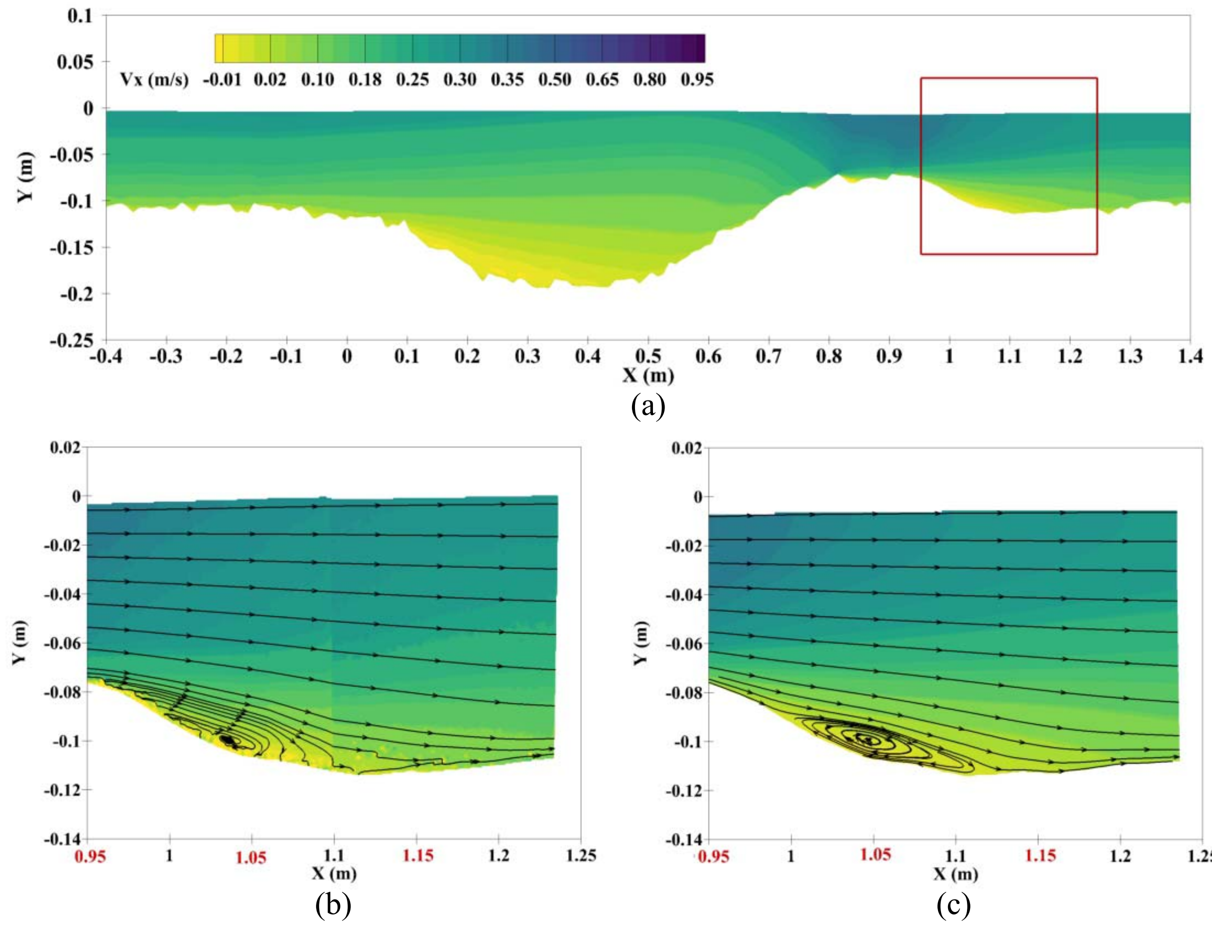

Figure 4: (a) Streamwise velocity field contours for the fast (0.2 m/s) flow case around the redd with the experimental and CFD comparison region indicated by the red square box. (b) Experimental and (c) CFD results. The red X-labels in (b) and (c) indicate the region where the velocity profiles are extracted. The flow direction is from left to right.

Comparison of the overall size of the separation vortex and reattachment locations shows a good agreement between the measured and predicted flow fields downstream of the redd (Figure 4b and Figure 4c). Similarly, when comparing the streamwise velocity (V_x) profiles just downstream of the crest (X = 0.95 m) and just downstream end of the redd (X = 1.05 m and X = 1.15 m), both flow cases yield very good NSC values of 0.84, 0.97, and 0.92 for fast flow, and 0.8, 0.98, and 0.9 for slow flow at X = 0.95 m, X = 1.05 m, and X = 1.15 m, respectively (Figure 5). These results are consistent with those obtained by Bhattarai et. al., (2023) (In Press) in their study for the same surface discharge that also exhibit very good NSC values.

Additionally, Bhattarai et al., (2023) (In Press) implemented the verification and validation for the same flow discharge as studied here, using the method developed by Xing and Stern (2008; 2010, 2011), and observed a monotonic convergence of solutions for the grid triplets, and yielded validated solutions at four different testing locations. These results underscore the capability of our CFD model to predict the flow field resulting from redd-flow interaction accurately.

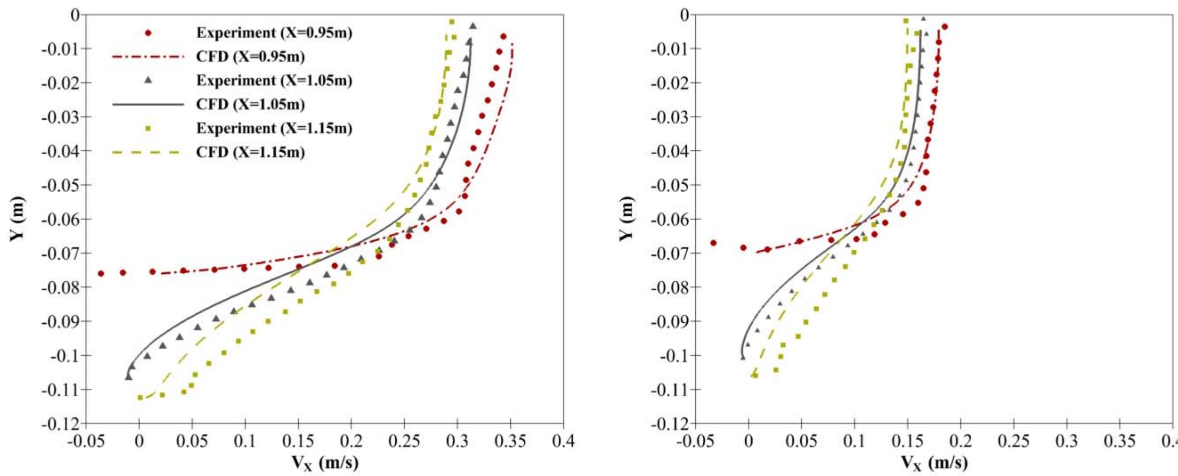

(a) (b)

Figure 5: Comparison between the simulated (solid and dashed lines) and experimental (symbols) streamwise velocity profiles at X = 0.95 m, 1.05 m, and 1.15 m for (a) fast (0.2 m/s), and (b) slow (0.1 m/s) flows. These specific locations are marked by red X-labels in Figure 4.

5. RESULTS

5.1 Effect of egg pocket permeability

The simulated interstitial streamlines converge toward the egg pocket as K_{EP}^* increases because of the increased flow velocity within the egg pocket (Figure 6). When $K_{EP}^* = 1$, water consistently flows into the egg pocket from the top and upstream sides, while exiting from the downstream and bottom sides, without deviating from the flow path. With $K_{EP}^* > 1$, most of the water enters the egg pocket from the upstream side and exits from the downstream side. Additionally, a portion of the water flow is diverted into the egg pocket from the top and bottom and exits from these sides as well. For the $K_{EP}^* = 8$, the inflow increased by about 71% from the case with $K_{EP}^* = 1$ (Figure 6f). Although the local egg pocket hydraulic conductivity has some impact, the primary control of the interstitial flow into the egg pocket is still predominantly governed by the overall permeability of the redd, because even the 8-fold increase in the egg pocket hydraulic conductivity (800% increase in permeability) results in only approximately a 71% increase in flow into the egg pocket, $\bar{q}_{ep}^*$.

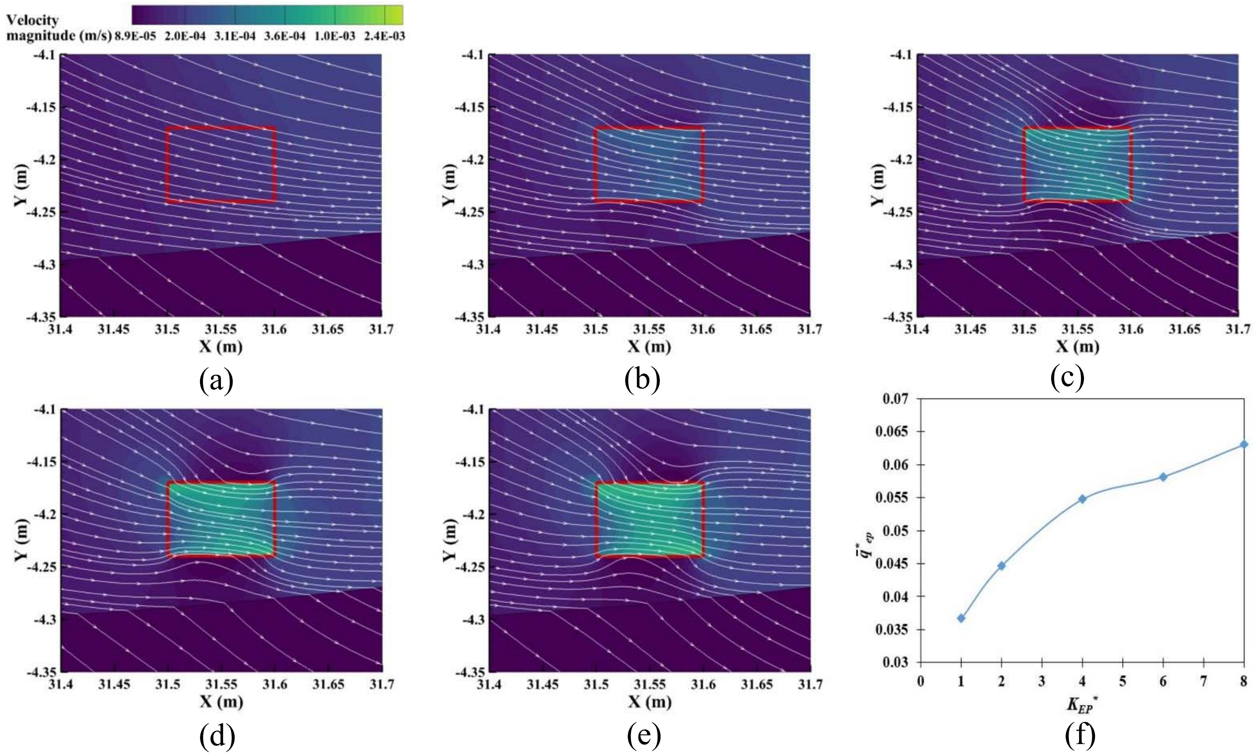

Figure 6: Flow streamlines in and around the egg pocket (EP_2) with different permeabilities for the smooth case (σ_E = 0). Their corresponding hydraulic conductivities (K_{EP}) are (a) $K_{EP} = K_D$, (b) $K_{EP} = 2 \cdot K_D$, (c) $K_{EP} = 4 \cdot K_D$, (d) $K_{EP} = 6 \cdot K_D$, and (e) $K_{EP} = 8 \cdot K_D$. (f) The flux entering the egg pocket, normalized by the disturbed bed hydraulic conductivity, $\bar{q}_{ep}^{*} = \frac{\bar{q}_{ep}}{K_D}$, where K_D = 0.0025 m/s, plotted against different normalized egg pocket hydraulic conductivities (${K_{EP}}^{*} = \frac{K_{EP}}{K_D}$).

5.2 Effect of egg pocket location

Interstitial flows passing through the egg pockets increase with the distance downstream of the redd pit from EP_1 to EP_5 (Figure 7). Specifically, egg pocket EP_5, located in the upwelling region, receives over five times the flux compared to EP_1. The flux entering each egg pocket at various locations is largely independent of the presence of additional egg pockets within the redd (Figure 7). The variations in interstitial flow entering any given egg pocket between simulations with or without additional egg pockets are minimal, amounting to less than ~9%, which could be due to the influence of adjacent egg pockets on the flow dynamics.

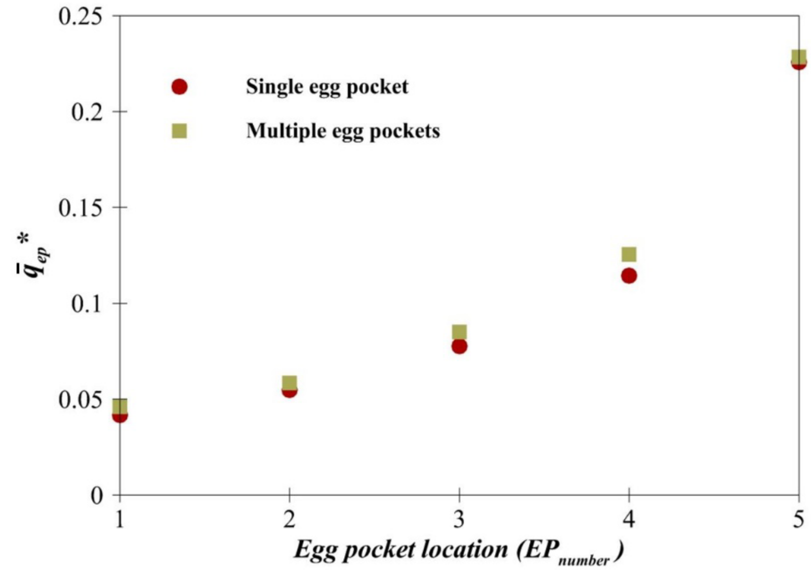

Figure 7: Normalized flow velocity entering the egg pocket ($\bar{q}^*_{ep} = \frac{\bar{q}_{ep}}{K_D}$, with K_D = 0.0025 m/s) at different egg pocket locations for the smooth case (σ_E = 0).

These results are further supported by visual inspection of the streamlines, which indicate similar trends for both single and multiple egg pockets. Moreover, there is a noticeable overall increase in interstitial flow as the egg pocket is positioned closer to the redd crest (Figure 8).

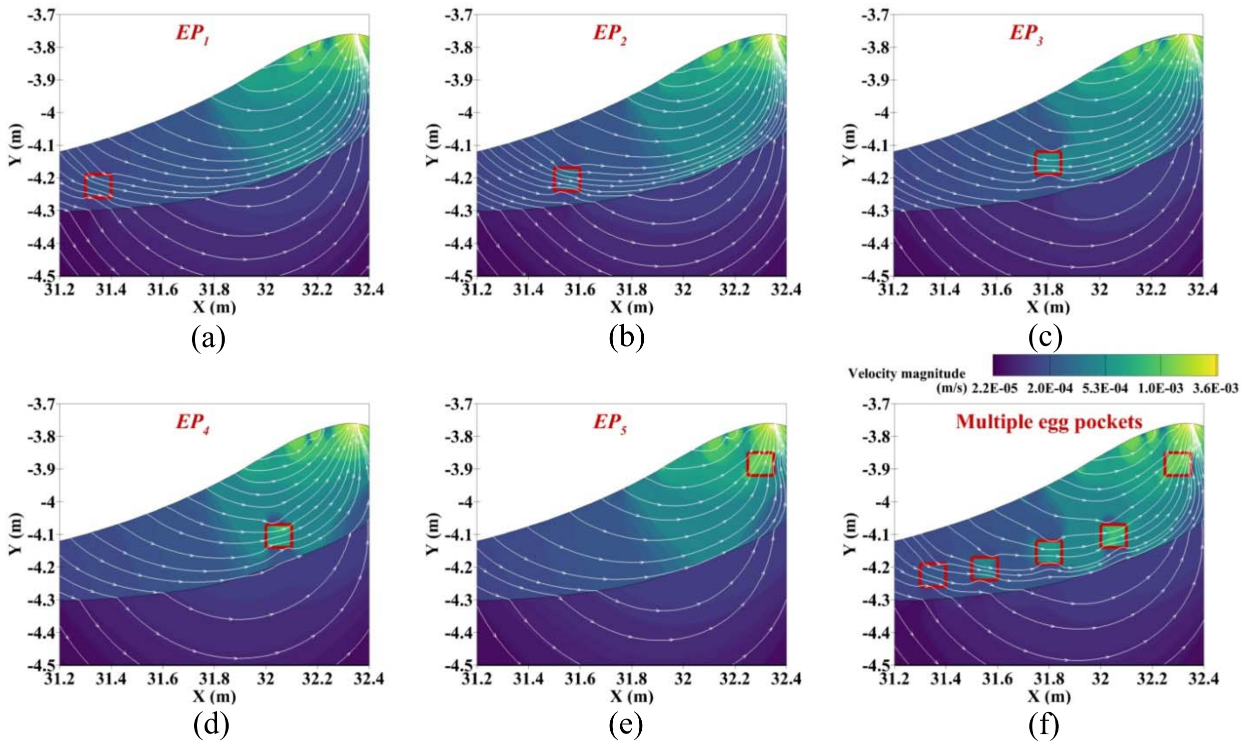

Figure 8: Visualization of flow streamlines for (a-e) individual egg pockets and (f) multiple egg pockets located at different positions within a single redd for the smooth case (σ_E = 0). All the egg pockets have the same hydraulic conductivity ($K_{EP} = 4 \cdot K_D$). Flow is from left to right.

5.3 Effects of bed roughness

The downwelling fluxes are influenced by the interaction between surface hydraulics and the redd shape with a smooth bed surface, as demonstrated by Bhattarai et al. (2023) (In Press). They showed that the relative total head drop (ΔH_R) between upstream and downstream locations of the redd, as well as the downwelling flux through the redd, increases with the discharge and the redd aspect ratio ($A_R = A/L$) for a smooth surface.

However, when the redd has a rough surface of type R_1, the ΔH_R decreases as R_1 increases, with the smooth bed exhibiting the largest ΔH_R (Figure 9a). This decrease in ΔH_R is attributed to local head variations that consume energy at the local level, resulting in a smaller overall relative total head drop. In contrast to the impact on ΔH_R observed with R_1 roughness, the case of R_2 roughness does not show a significant difference in ΔH_R compared to the smooth bed case. However, the head profiles do exhibit oscillations around the head profile of the smooth bed due to localized head variations (Figure 9b).

Superimposed onto the redd-induced head profile, there are localized small head drops that occur at the roughness scales that result in numerous localized hyporheic cells formed within the larger hyporheic cell between the pit and tailspill (Figure 10a). This highlights the fact that an increase in vertical roughness (R_1) leads to the formation of local hyporheic cells, with the size of these cells growing as R_1 increases. The local hyporheic flow cells due to grain roughness are much shallower and subdued for R_2 compared to R_1 (c.f., Figure 10a and b). For a smooth bed, the flow above the egg pocket downwells from the area between the pit and the tailspill (stoss side of the redd) directly entering the egg pocket. However, when the bed is rough, it can significantly influence the flow direction, potentially causing the flow to enter the egg pocket from a different zone. As the spatial distribution of roughness can vary randomly due to sediment transport, this variability can affect the origin of the flowline entering the egg pockets. In certain cases, the presence of roughness can amplify the effect of the redd topography, resulting in a small area of the redd surface contributing most of the flow that enters the egg pocket. This is illustrated in Figure 10a, where the flow entering the egg pocket originates from the bottom of the pit. The control of roughness on the flow path is less noticeable for R_2 (Figure 10b).

The downwelling flow at the water-sediment interface increases with R_1 (Figure 11) primarily due to shallow and fast roughness-scale hyporheic flow cells, as previously observed in rough beds but without a redd (Reidenbach et al., 2010). The depth of penetration of these localized hyporheic flow cells becomes larger and faster with increasing R_1 roughness (Figure 10a), because of the increase in local head drops (Figure 9a). Conversely, the downwelling fluxes are negligibly affected by R_2 roughness (Figure 11).

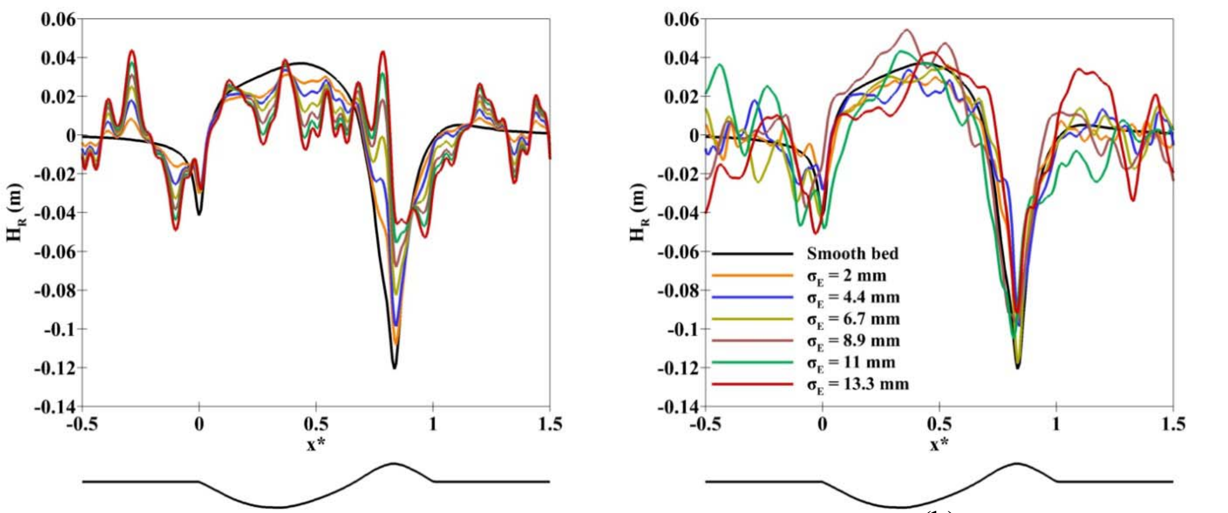

(a) (b)

Figure 9: Relative total head (H_R) as a function of dimensionless distance (x^*), defined as the distance normalized by the redd wavelength ($x^* = \frac{x}{L}$), over the redds of roughness types (a) R_1 and (b) R_2, along with the corresponding illustration of the smooth redd profile indicating redd location. Flow is from left to right.

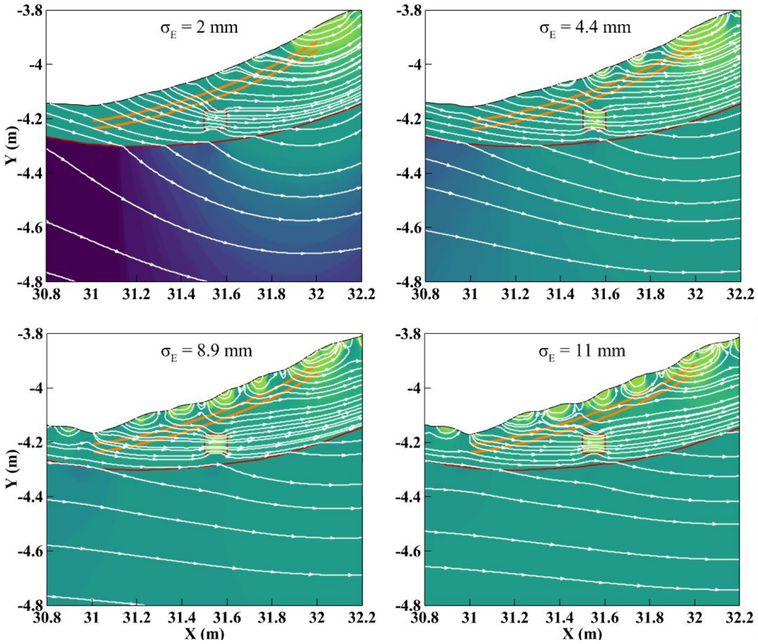

(a)

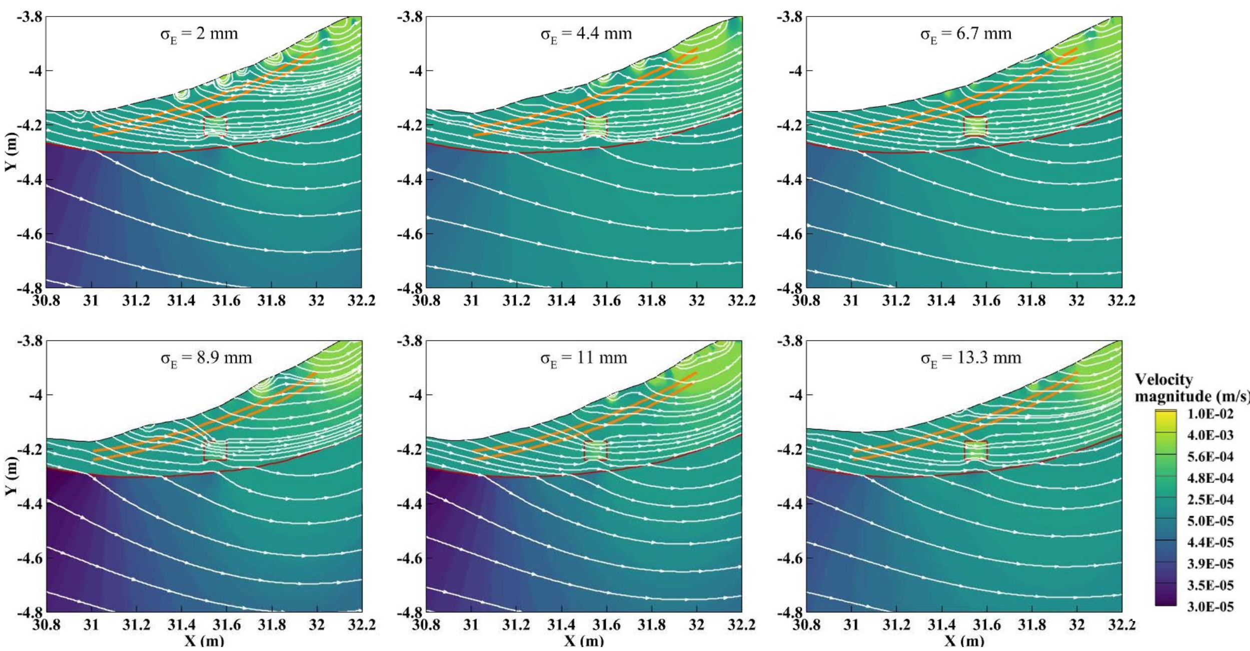

(b)

Figure 10: Subsurface flow characteristics for different stream bed roughness (a) R_1 and (b) R_2 with egg pocket (EP_2) of hydraulic conductivity, $K_{EP} = 4 \cdot K_D$, situated inside the redd. The orange curves indicate the locations at which downwelling fluxes are extracted at 2 times (top) and 3 times the D_{50} of a 3 cm roughness. Flow is from left to right.

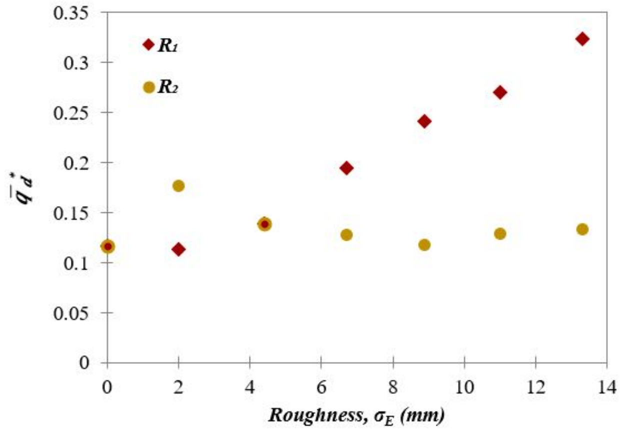

Figure 11: Average downwelling velocity normalized by the disturbed bed hydraulic conductivity, $\bar{q}_d^* = \frac{\bar{q}_d}{K_D}$, over the entire redd for two types of rough beds, R_1 (diamond) and R_2 (circle).

The interstitial flow velocity gradually decreases further into the redd. The downwelling flow velocity at the water-sediment interface is nearly two times higher than at regions $2{\cdot}D_{50}$ (6 cm) and $3{\cdot}D_{50}$ (9 cm) below the smooth bed surface (Figure 12). Moreover, the flow velocity at $2{\cdot}D_{50}$ is slightly higher than that at $3{\cdot}D_{50}$ (Figure 12b), indicating that most of the flow reduction occurs within the first shallow band of $2{\cdot}D_{50}$. Notably, the flow at $3{\cdot}D_{50}$ is minimally influenced by the type and amount of roughness (Figure 12b). Consequently, the surface roughness may have a negligible effect on the flux directed toward the egg pockets.

In our comparison of the downwelling flow between the two rough beds (R_1 and R_2 of σ_E = 13.3 mm), we found that the average downwelling flow in the region that affects the egg pocket significantly varied at the water-sediment interface (Figure S3). However, deeper within the redd, the mean downwelling flow variation was not substantial. At the water-sediment interface, the average downwelling flows, $\bar{q}_{d,ep}$, for R_1 and R_2 were observed to be 0.73 mm/s and 0.3 mm/s, respectively (Figure 12a). However, at a depth of $2{\cdot}D_{50}$, the variations in average downwelling flows, $\bar{q}_{d,2d,ep}$, were smaller, with the values of 0.16 mm/s and 0.14 mm/s for R_1 and R_2, respectively. Further, at a depth of $3{\cdot}D_{50}$, the average downwelling flows, $\bar{q}_{d,3d,ep}$, for R_1 and R_2 were similar, with the values of 0.12 mm/s and 0.127 mm/s, respectively (Figure 12b). Therefore, the impact of varying surface roughness types on the average downwelling flow becomes less significant deeper within the redd, with negligible variations of less than 6% for $\bar{q}_{d,3d,ep}$.

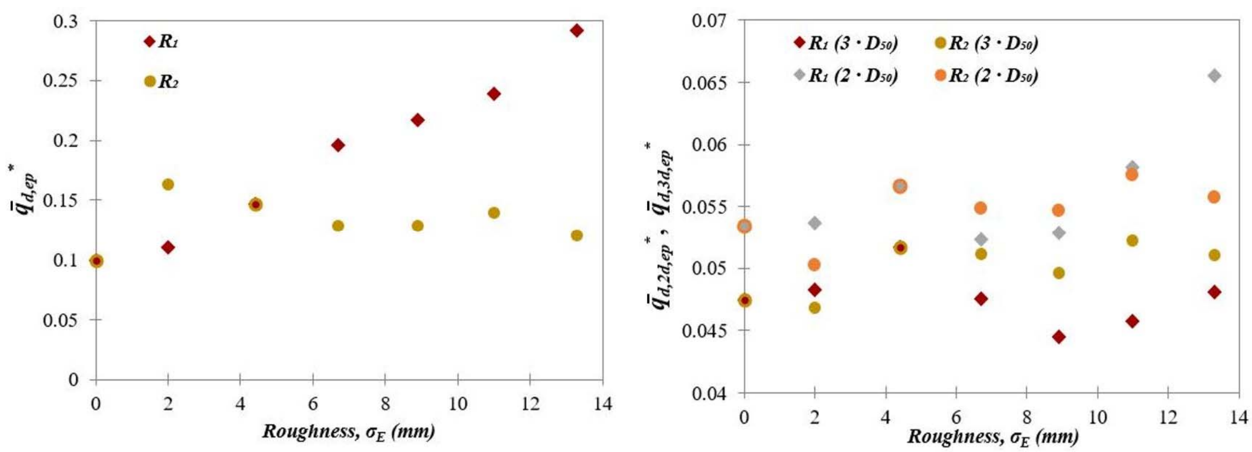

(a) (b)

Figure 12: Average downwelling velocity normalized by the disturbed bed hydraulic conductivity over the region between pit and tailspill with egg pocket hydraulic conductivity, $K_{EP} = 4{\cdot}K_D$, at (a) water-sediment interface ($\bar{q}_{d,ep}^* = \frac{\bar{q}_{d,ep}}{K_D}$) and at (b) $2{\cdot}D_{50}$ ($\bar{q}_{d,2d,ep}^* = \frac{\bar{q}_{d,2d,ep}}{K_D}$) and, $3{\cdot}D_{50}$ ($\bar{q}_{d,3d,ep}^* = \frac{\bar{q}_{d,3d,ep}}{K_D}$).

Although the hyporheic flux entering an egg pocket, $\bar{q}_{ep}^*$, initially increased with bed roughness, this increase may be different from the 6% that was quantified for the spatially averaged downwelling flow at a depth of $3{\cdot}D_{50}$. For instance, its value oscillates at around a 45% increase compared to the smooth bed for both types of roughness for EP_2 (Figure 13a).

The impact of $K_{EP}{}^{*}$ on $\bar{q}^{*}_{ep}$ increase from 71% for smooth bed to 92% for a bed with roughness with σ_E = 4.4 mm, when $K_{EP}{}^{*}$ is increased by 8-folds (Figure 13b). This further supports the observation that the overall redd hydraulic conductivity primarily controls the overall flow through the egg.

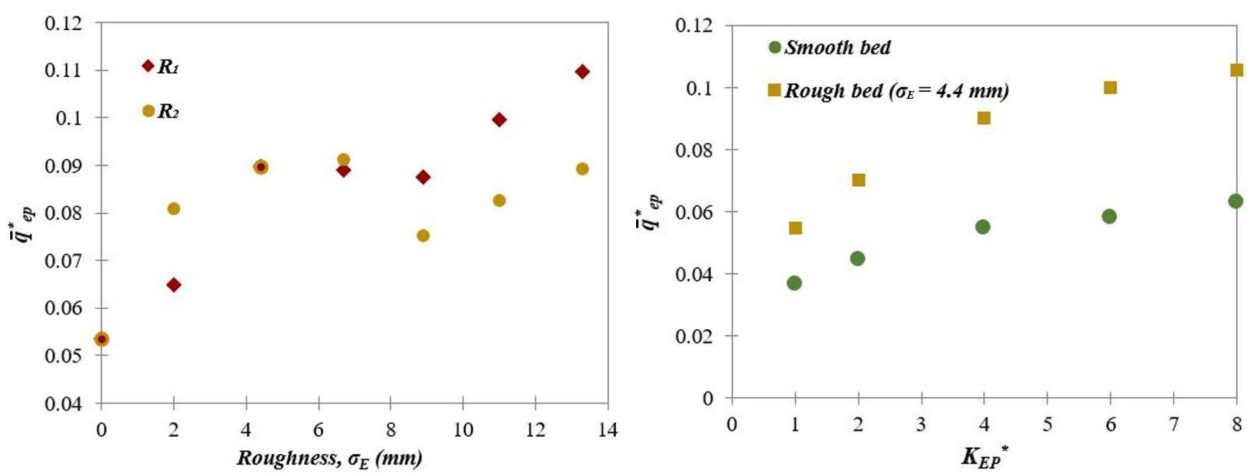

(a) (b)

Figure 13: (a) Normalized flux ($\bar{q}^{*}_{ep} = \frac{\bar{q}_{ep}}{K_D}$) entering the egg pocket, EP_2, of hydraulic conductivity $K_{EP} = 4 \cdot K_D$ plotted against rough waterbeds R_1 (diamond) and R_2 (circle), and (b) Normalized flux ($\bar{q}^{*}_{ep} = \frac{\bar{q}_{ep}}{K_D}$) entering the egg pocket, EP_2, plotted against different normalized hydraulic conductivities ($K_{EP}{}^{*} = \frac{K_{EP}}{K_D}$).

6. DISCUSSION

Previous studies have investigated the effect of the interaction between surface hydraulics and redd shape and size (Bhattarai et al., 2023; Cardenas et al., 2016; Tonina & Buffington, 2009). The recent work of Bhattarai et al. (2023) (In Press) shows an increase in mean downwelling hyporheic flux with stream discharge and redd aspect ratio. An increase in stream discharge results in an order of magnitude increase in the downwelling fluxes, while an increase in redd aspect ratio results in several tens of percent increase in the downwelling fluxes. The redd hydraulic conductivity is also a significant controlling factor that exhibits a linear impact on the fluxes. Tonina and Buffington (2009) showed that the increased permeability of the redd sediment due to spawning activity has a primary impact on the interstitial fluxes. Furthermore, Bhattarai et al. (2023) (In Press) showed that the redd permeability controls the redd-induced hyporheic fluxes, regardless of the undisturbed streambed permeability. Our analysis revealed a secondary impact, where the increased permeability of the egg pocket, in comparison to the overall redd permeability, contributes to the heterogeneity and the additional permeability observed within the redd. Specifically, an 8x (800%) increase in the egg pocket permeability compared to the redd permeability leads to a 71% increase in the mean flux entering the eggs. Here, we estimate that the egg pocket permeability, K_{EP}, is higher than that of the overall redd permeability because of the accumulation of large particles that form the structure of the egg pocket. However, female salmon lay their eggs in large numbers within the large interstices, which may substantially reduce the egg pocket permeability. This effect has not yet been quantified to the best of our knowledge. Thus, K_{EP} values may be similar to those of the overall redd. K_{EP} effect is also smaller than that of the effect due to the egg pocket location within the redd. The location of the egg pocket within the redd can significantly vary, resulting in several-fold changes in the interstitial flow entering the eggs.

Egg pockets can exist at multiple locations within a redd, and they experience different interstitial flows. Shallower egg pockets may experience higher $\bar{q}_{ep}^{*}$ compared to deeper egg pockets, but they may also face a higher risk of being excavated by erosion during high flows. The variability in predicted interstitial flows may be significantly influenced by the uncertainty surrounding the location of the egg pocket, more so than the hydraulic conductivity attributed to the egg pocket itself. Within the range of egg pocket locations studied in this research, this uncertainty can be as much as five times higher than the variability caused by ${K_{EP}}^* > 1$. Moreover, this level of uncertainty is larger than the influence of surface roughness on $\bar{q}_{ep}^*$. Whereas here we studied 5 egg pocket locations, future research could provide better constrains on the impact of egg pocket hydraulic conductivity, the number of egg pockets within the redd, and their spatial arrangement on hyporheic fluxes.

Salmonids may spawn in streambeds with a wide range of sediment, ranging from fine gravel to cobbles, which can result in significant variations in surface roughness. Spawning activity, whether in high or low densities, has the potential to modify streambeds through sediment mixing (Gottesfeld et al., 2004), fines purging (DeVries, 2012), coarsening and sorting of surface grains (Kondolf & Wolman, 1993), and loosening of grain packing (Montgomery et al., 1996). These alterations are beneficial for salmon reproduction success as they promote hyporheic flow that oxygenates eggs and removes metabolic waste from egg pits (Chapman, 1988; Tonina & Buffington, 2009). Our results show that bed surface roughness has a discernible effect on the downwelling flow only at the water-sediment interface. At the roughness scale, locally generated pressure gradients give rise to small and shallow hyporheic exchange cells. In flat beds, Dudunake (2020) showed that grain roughness may generate mean hyporheic depths up to 26 times the median grain size, whereas, our study shows that the redd shape constrains these fluxes to a superficial layer that is approximately twice the median grain size. The current study builds upon these findings by demonstrating that the impact of streambed roughness on interstitial flows near the egg pockets is primarily controlled by the redd shape, regardless of roughness type (R_1 or R_2). Thus, roughness-induced hyporheic flows may not reach the egg pockets, whose interstitial flux, $\bar{q}_{ep}^*$, is chiefly driven by the redd shape. However, the impact of roughness on

$\bar{q}^*_{ep}$ depends on egg pocket location. Potentially, species with smaller redds, where egg pockets are located at shallower sediment depths compared to Chinook salmon redds, may benefit from roughness-induced flows. Nevertheless, smaller fish typically spawn in less coarse sediment than Chinook salmon, and their redds may have higher aspect ratios, potentially constraining the roughness-induced hyporheic flows. The potential for variability in this relationship across different roughness types and redd shapes has not been thoroughly investigated. Therefore, future work could explore this further by comparing the effects of different roughness types on hyporheic fluxes across a range of redd shapes.

Building on the study of Bhattarai et al., (2023) (In Press), which suggests that overall shape of the redd impacts the flow rate into the egg pocket, our study adds that the flow rate is also influenced by the redd hydraulic conductivity and the position of the egg pocket. Analysis based on a smooth redd surface with a single redd hydraulic conductivity may provide a good indication of the mean downwelling fluxes which the egg pocket may experience. For instance, the normalized downwelling flux for the smooth case, σ_E = 0, ($\bar{q}^*_{d,ep}$ = 0.1) (Figure 12a) is similar to the flux into EP_2 for the roughest bed, σ_E = 13.3 mm, ($\bar{q}^*_{ep}$= 0.11) (Figure 13a) and highest egg pocket permeability analyzed in this study. The equations for predicting downwelling flux proposed by Bhattarai et al., (2023) (In Press) were used to quantify $\bar{q}^*_{d,ep}$. These values are then affected by uncertainty due to surface roughness and egg-pocket permeability and locations. These uncertainties could be estimated with the analysis provided here. Our analysis suggests that egg pocket location uncertainty has the larger impact on $\bar{q}^*_{ep}$ variability than egg pocket permeability and surface roughness.

7. CONCLUSION

Salmonids protect and nurture their eggs by placing them in streambed gravel and shaping their nests as a dune, which induces the flow of oxygen-rich surface water toward their egg pockets. The egg pockets within the redd may have different locations and potentially higher hydraulic conductivities compared to the overall redd. Additionally, the presence of streambed gravel creates rough surfaces, which can modify the downwelling fluxes influenced by the shape of the redd.

Our simulations show that the interstitial flows towards the egg pocket increase toward the tailspill crest with egg pocket distance from the pit. The downstream pockets, EP_2, EP_3, EP_4, and EP_5, receive roughly 1.3, 2, 3, and 5.4 times higher fluxes, respectively, compared to EP_1. This density of egg pockets shows no hydraulic interference, such that the fluxes within each egg pocket, simulated individually or as a group, are similar.

The impact of the difference in hydraulic conductivity between the egg pocket and the overall redd permeability leads to an increase in interstitial flow towards the egg pocket. However, this increase is relatively small compared to the egg pocket location uncertainty. For instance, an eight-fold increase in the egg pocket permeability compared to that of the redd results in a 71% increase in interstitial flow. This increase, though beneficial, is considered minor when compared to the uncertainties associated with redd hydraulic conductivities and the location of the egg pocket.

Near-bed pressure gradients depend on the roughness of the streambed. Generally, rough streambeds lead to more complex hyporheic exchanges, characterized by the presence of multiple fast and shallow near-surface hyporheic cells superimposed over those generated by the redd shape. This phenomenon is more pronounced in R_1 roughness compared to R_2 roughness. The impact of streambed roughness is small in the sediment depths that are twice the median grain size, which typically represents the thickness of the armor layer in the streambed sediment. Reaching sediment depths of $3 \cdot D_{50}$, the impact of roughness becomes negligible, regardless of roughness type (R_1 or R_2). Consequently, the interstitial flows near the egg pockets are chiefly controlled by the redd shape. The redd shape and permeability remain the key factors driving the flow into the egg pocket.

Overall, our results suggest that the common simplification of the redd as a single homogenous feature with a smooth surface captures the primary mechanisms that drive the transport of oxygen-rich surface water toward the eggs. Information on egg pocket hydraulic conductivity, egg pocket location, and surface roughness could be used to define the natural variability around the estimated downwelling fluxes by a smooth bed with a single hydraulic conductivity, as proposed by Bhattarai et al., (2023) (In Press).

Acknowledgment

This research has been supported by the grant 19-028-300 California State Water Resources Control Board. We would like to thank Andrew Pike who shared the coupled velocity-depth data at redd locations along the Sacramento River, quantified in the Winter-run Chinook salmon Lifecycle model project. Equipment used for experiments was supported by the National Science Foundation (NSF Grant 2043382). All data have been reported in the hydroshare repository Bhattarai et al. (2022), http://www.hydroshare.org/resource/6deaf594de954b95b81bd117bd919960.

REFERENCES

Aberle, J., & Nikora, V. (2006). Statistical properties of armored gravel bed surfaces. *Water Resources Research*, *42*(11), 1–11. https://doi.org/10.1029/2005WR004674

Baxter, C. V., & Hauer, F. R. (2000). Geomorphology, hyporheic exchange, and selection of spawning habitat by bull trout (Salvelinus confluentus). *Canadian Journal of Fisheries and Aquatic Sciences*, *57*(7), 1470–1481. https://doi.org/10.1139/f00-056

Van Den Berghe, E. P., & Gross, M. R. (1984). Female size and nest depth in coho salmon (Oncorhynchus kisutch). *Canadian Journal of Fisheries and Aquatic Sciences*, *41*(1), 204–206. https://doi.org/10.1139/f84-022

Bhattarai, B., Hilliard, B., Reeder, W. J., Budwig, R., Martin, T., Xing, T., & Tonina, D. (2023). Effect of surface hydraulics and salmon redd size on redd-induced hyporheic exchange. *Water Resources Research (In Press)*, 0–42. https://doi.org/10.1002/essoar.10512760.1

Bjornn, T. C., & Reiser, D. W. (1991). Habitat requirements of salmonids in streams. In W. R. Meehan (Ed.), *Influence of forest and rangeland management on salmonid fishes and their habitats* (pp. 83–138). Am. Fish. Soc. Spec. Publ. 19. Bethesda, Md.

Burner, C. J. (1951). Characteristics of spawning nests of Columbia River salmon. *Fishery Bulletin*, *52*, 97–110.

Cardenas, Ford, A. E. A., Kaufman, M. H., Kessler, A. J., Cook, P. L. M., … M. K.-J. of, & 2016, U. (2016). Hyporheic flow and dissolved oxygen distribution in fish nests: The effects of open channel velocity, permeability patterns, and groundwater upwelling. *Journal of Geophysical Research: Biogeosciences*, *121*(12), 3113–3130. https://doi.org/10.1002/2016JG003381

Cardenas, M. B., & Wilson, J. L. (2007a). Effects of current-bed form induced fluid flow on the thermal regime of sediments. *Water Resources Research*, *43*(8), 1–12. https://doi.org/10.1029/2006WR005343

Cardenas, M. B., & Wilson, J. L. (2007b). Hydrodynamics of coupled flow above and below a sediment-water interface with triangular bedforms. *Advances in Water Resources*, *30*(3), 301–313. https://doi.org/10.1016/j.advwatres.2006.06.009

Chapman, D. W. (1988). Critical Review of Variables Used to Define Effects of Fines in Redds of Large Salmonids. *Transactions of the American Fisheries Society*, *52*(8), 567. https://doi.org/10.1097/00006324-197508000-00010

Chen, X., Cardenas, M. B., & Chen, L. (2015). Three-dimensional versus two-dimensional bed form-induced hyporheic exchange. *Water Resources Research*, *51*, 2923–2936. https://doi.org/10.1002/ 2014WR016848

Coble, D. W. (1961). Influence of Water Exchange and Dissolved Oxygen in Redds on Survival of Steelhead Trout Embryos. *Transactions of the American Fisheries Society*, *90*(4), 469–474. https://doi.org/10.1577/1548-8659(1961)90[469:iowead]2.0.co;2

Cooper, J. R., & Tait, S. J. (2009). Water-worked gravel beds in laboratory flumes – a natural analogue? *Earth Surface Processes and Landforms*, *34*, 613–628. https://doi.org/10.1002/esp.1743

Crisp, D. T., & Carling, P. A. (1989). Observations on siting, dimensions, and structure of salmonid redds. *Journal of Fish Biology*, *34*, 119–134.

Deverall, K. R., Kelso, J. R. M., & James, G. D. (1993). Redd characteristics and implications for survival of chinook salmon (Oncorhynchus tshawytscha) embryos in the Waitaki river, New Zealand. *New Zealand Journal of Marine and Freshwater Research*, *27*(4), 437–444. https://doi.org/10.1080/00288330.1993.9516585

DeVries, P. (2012). Salmonid influences on rivers: A geomorphic fish tail. *Geomorphology*, *157–158*, 66–74. https://doi.org/10.1016/j.geomorph.2011.04.040

Dudunake, T., Tonina, D., Reeder, W. J., & Monsalve, A. (2020). Local and Reach-Scale Hyporheic Flow Response From Boulder-Induced Geomorphic Changes. *Water Resources Research*, *56*(10). https://doi.org/10.1029/2020WR027719

Elliott, J. M. (1984). Numerical Changes and Population Regulation in Young Migratory Trout Salmo trutta in a Lake District Stream , 1966-83. *Journal of Animal Ecology*, *53*(1), 327–350. Retrieved from https://www.jstor.org/stable/4360

Evenson, D. F. (2001). *Egg pocket depth and particle size composition within chinook salmon redds in the trinity river*. Humboldt State University.

Geist, D. R. (2000). Hyporheic discharge of river water into fall chinook salmon (Oncorhynchus. *Methods*.

Gottesfeld, A. S., Hassan, M. A., Tunnicliffe, J. F., & Poirier, R. W. (2004). Sediment dispersion in salmon spawning streams: The influence of floods and salmon redd construction. *Journal of the American Water Resources Association*, *40*(4), 1071–1086. https://doi.org/10.1111/j.1752-1688.2004.tb01068.x

Greig S. M., Sear D. A., & Carling, P. A. (2006). A review of factors influencing the availability of dissolved oxygen to incubating salmonid embryos. *HYDROLOGICAL PROCESSES*, *21*, 323–334. https://doi.org/10.1002/hyp.6188 A

Groot, C., & Margolis, L. (1991). *Pacific salmon life histories*. Vancouver, Canada: Columbia Press.

Hanrahan, T. P., Geist, D. R., & Arntzen, E. V. (2005). Habitat quality of historic snake river fall chinook salmon spawning locations and implications for incubation survival part 1:

Substrate quality. *River Research and Applications*, *21*(5), 455–467. https://doi.org/10.1002/rra.823

Hawke, S. P. (1978). Stranded redds of quinnat salmon in the mathias river, South Island, New Zealand. *New Zealand Journal of Marine and Freshwater Research*, *12*(2), 167–171. https://doi.org/10.1080/00288330.1978.9515737

Heritage, G. L., & Milan, D. J. (2009). Terrestrial Laser Scanning of grain roughness in a gravel-bed river. *Geomorphology*, *113*(1–2), 4–11. https://doi.org/10.1016/j.geomorph.2009.03.021

Hervant, F., & Malard, F. (1999). Oxygen supply and the adaptations of animals in groundwater. *Freshwater Biology*, *41*(1), 1–30. https://doi.org/10.1046/j.1365-2427.1999.00379.x

Janssen, F., Cardenas, M. B., Sawyer, A. H., Dammrich, T., Krietsch, J., & De Beer, D. (2012). A comparative experimental and multiphysics computational fluid dynamics study of coupled surface-subsurface flow in bed forms. *Water Resources Research*, *48*(8), 1–16. https://doi.org/10.1029/2012WR011982

Keulegan, G. H. (1938). Laws of turbulent flow in open channels. *Journal of Research of the National Bureau of Standards*, *21*(6), 707. https://doi.org/10.6028/jres.021.039

Kondolf, G. M. (2000). Assessing Salmonid Spawning Gravel Quality. *Transactions of the American Fisheries Society*, *129*(1), 262–281. https://doi.org/10.1577/1548-8659(2000)129<0262:assgq>2.0.co;2

Kondolf, G. M., & Wolman, M. G. (1993). The sizes of salmonid spawning gravels. *Water Resources Research*, *29*(7), 2275–2285. https://doi.org/10.1029/93WR00402

Lee, A., Aubeneau, A. F., & Cardenas, M. B. (2020). The Sensitivity of Hyporheic Exchange to Fractal Properties of Riverbeds. *Water Resources Research*, *56*(5), 1–15.

https://doi.org/10.1029/2019WR026560

Maekawa, K., & Hino, T. (1990). Spawning tactics of female Miyabe charr (Salvelinus malma miyabei) against egg cannibalism. *Canadian Journal of Zoology*, *68*(5), 889–894. https://doi.org/10.1139/z90-129

McNeil, W. J., & Ahnell, W. H. (1964). SUCCESS OF PINK SALMON SPAWNING RELATIVE TO SIZE OF SPAWNING BED MATERIALS. *US Fish and Wildlife Service, Special Scientific Report-Fisheries No. 469*, (157), 1–15. Retrieved from http://spfgtsn.krisweb.com/biblio/gen_usfws_mcneiletal_1964.pdf

Mendoza, C., & Zhou, D. (1992). Effects of porous bed on turbulent stream flow above bed. *Journal of Hydraulic Engineering*, *118*(9), 1222–1240.

Merz, J. E., Setka, J. D., Pasternack, G. B., & Wheaton, J. M. (2004). Predicting benefits of spawning-habitat rehabilitation to salmonid (Oncorhynchus spp.) fry production in a regulated California river. *Canadian Journal of Fisheries and Aquatic Sciences*, *61*(8), 1433–1446. https://doi.org/10.1139/F04-077

Montgomery, D. R., Buffington, J. M., Peterson, N. P., Schuett-Hames, D., & Quinn, T. P. (1996). Stream-bed scour, egg burial depths, and the influence of salmonid spawning on bed surface mobility and embryo survival. *Canadian Journal of Fisheries and Aquatic Sciences*, *53*(5), 1061–1070. https://doi.org/10.1139/f96-028

Moriasi, D. N., Arnold, J., Van Liew, M., Bingner, R., Harmel, D., & Veith, T. (2007). Model evaluation guidelines for systematic quantification of accuracy in watershed simulations. *Transactions of the American Society of Agricultural and Biological Engineers*, *50*(3), 885–900.

Nikora, V. I., Goring, D. G., & Biggs, B. J. F. (1998). On gravel-bed roughness characterization, *34*(3), 517–527.

Peterson, N. P., & Quinn, T. P. (1996). Persistence of egg pocket architecture in redds of chum salmon, Oncorhynchus keta. *Environmental Biology of Fishes*, *46*(3), 243–253.

Reidenbach, M. A., Limm, M., Hondzo, M., & Stacey, M. T. (2010). Effects of bed roughness on boundary layer mixing and mass flux across the sediment-water interface. *Water Resources Research*, *46*(7). https://doi.org/10.1029/2009WR008248

Smart, G., Aberle, J., Duncan, M., & Walsh, J. (2004). Measurement and analysis of alluvial bed roughness. *Journal of Hydraulic Research*, *42*(3), 227–237. https://doi.org/10.1080/00221686.2004.9728388

Tappel, P. D., & Bjornn, T. C. (1983). A New Method of Relating Size of Spawning Gravel to Salmonid Embryo Survival. *North American Journal of Fisheries Management*, *3*(2), 123–135. https://doi.org/10.1577/1548-8659(1983)3<123:anmors>2.0.co;2

Tonina, D., & Buffington, J. M. (2009). A three-dimensional model for analyzing the effects of salmon redds on hyporheic exchange and egg pocket habitat. *Canadian Journal of Fisheries and Aquatic Sciences*, *66*(12), 2157–2173. https://doi.org/10.1139/F09-146

Whiting, P. J., & Dietrich, W. E. (1991). Convective accelerations and boundary shear stress over a Channel Bar. *Water Resources Research*, *27*(5), 783–796. https://doi.org/10.1029/91WR00083

Wiberg, P. L., & Smith, J. D. (1991). Velocity distribution and bed roughness in high-gradient streams. *Water Resources Research*, *27*(5), 825–838. https://doi.org/10.1029/90WR02770

Xing, T., & Stern, F. (2010). Factors of safety for Richardson extrapolation. *Journal of Fluids Engineering, Transactions of the ASME*, *132*(6), 0614031–0640313. https://doi.org/10.1115/1.4001771

Xing, T., & Stern, F. (2011). Closure to “discussion of ‘factors of safety for Richardson Extrapolation’” (2011, ASME J. Fluids Eng., 133, p. 115501). *Journal of Fluids Engineering, Transactions of the ASME*, *133*(11), 2–7. https://doi.org/10.1115/1.4005030

Xing, T., Carrica, P., & Stern, F. (2008). Computational towing tank procedures for single run curves of resistance and propulsion. *Journal of Fluids Engineering, Transactions of the ASME*, *130*(10), 1011021–10110214. https://doi.org/10.1115/1.2969649

Zhou, D., & Mendoza, C. (1993). Flow through porous bed of turbulent stream. *Journal of Engineering Mechanics*, *119*(2), 365–383.

Zimmermann, A. E., & Lapointe, M. (2005a). Intergranular flow velocity through salmonid redds: Sensitivity to fines infiltration from low intensity sediment transport events. *River Research and Applications*, *21*(8), 865–881. https://doi.org/10.1002/rra.856

Zimmermann, A. E., & Lapointe, M. F. (2005b). Sediment infiltration traps: Their use to monitor salmonid spawning habitat in headwater tributaries of the Cascapédia River, Québec. *Hydrological Processes*, *19*(20), 4161–4177. https://doi.org/10.1002/hyp.5879